nature communications

Article

https://doi.org/10.1038/s41467-024-50746-7

High energy resolution $CsPbBr_3$ alpha particle detector with a full-customized readout application specific integrated circuit

Received: 3 January 2024

Accepted: 22 July 2024

Published online: 27 July 2024

Check for updates

Xin Zhang[1,2], Ruichen Bai[1,2], Yuhao Fu[3], Yingying Hao[1,2], Xinkai Peng[1,2], Jia Wang[2,3] ✉, Bangzhi Ge[1,2], Jianxi Liu[1], Yongcai Hu[2,4], Xiaoping Ouyang[5] ✉, Wanqi Jie[1,2] & Yadong Xu[1,2] ✉

α particles must be monitored to be managed as radioactive diagnostic agents or nuclear activity indicators. The new generation of perovskite detectors suffer from limited energy resolution, which affects spectroscopy and imaging applications. Here, we report that the solution-grown $CsPbBr_3$ crystal exhibits a low and stable dark current (34.6 nA·cm^{-2} at 200 V) by thinning the as-grown crystal to decrease the high concentration $CsPb_2Br_5$ phase near the surface. The introduction of the Schottky electrode for the $CsPbBr_3$ detector further reduces the dark current and improves the high-temperature stability. An energy resolution of 6.9% is achieved with the commercial electronic system, while the effects of air scattering and absorption are investigated. Moreover, 1.1% energy resolution is recognized by a full-customized readout application-specific integrated circuit without any additional signal processing, which matches well with the given parameters of the $CsPbBr_3$ detector by reducing the parasitic capacitance and electronic noise.

The development of detectors for heavy particles has been a long-standing research topic, not only for applications in nuclear safety[1], deep space exploration[2], and homeland security[3], but also for high-energy particle measurements. For instance, actinides play a crucial role as essential raw materials for nuclear reactors and weapons. The α particle, which acts as a key characteristic of actinides, holds significance in the field of radiation detection. Despite α particles are generally lower than that of beta particles or gamma rays, and can be effectively stopped by a piece of paper or human skin. However, it remains highly damaging due to ionizing radiation. When α-emitting atoms are inhaled, ingested, or injected into our body, the DNA would be damaged seriously, approximately 20 times greater than that induced by equivalent doses of beta particles or gamma rays[1,4–6]. Additionally, the radon (decay by emitting α particles) can potentially lead to lung cancer when ingested or inhaled and must be quantified to mitigate the exposure risk[5], which is an odorless, invisible gas naturally released from rocks, soil, and water. On the other hand, monitoring of high concentrations of α particle contaminations is an important issue for the decommissioning of the Fukushima Daiichi Nuclear Power Plant. The detection and radioactivity metrology of α particle is getting crucial, as demonstrated by the recurrent updates of regulations that for increasingly more sensitive and high-performance detectors[2].

So far, the fundamental principle of α particles interacting with materials has led to the invention of various types of detectors, such as gaseous ionization detectors, scintillation detectors and semiconductor

[1]School of Materials Science and Engineering, Northwestern Polytechnical University, Xi'an 710072, PR China. [2]Key Laboratory of Radiation Detection Materials and Devices, Ministry of Industry and Information Technology, Xi'an 710072, PR China. [3]School of Electronics and Information, Northwestern Polytechnical University, Xi'an 710072, PR China. [4]School of Computer Science, Northwestern Polytechnical University, Xi'an 710072, PR China. [5]Northwest Institute of Nuclear Technology, Xi'an 710024, PR China. ✉e-mail: jwang@nwpu.edu.cn; oyxp2003@aliyun.com; xyd220@nwpu.edu.cn

detectors[7–10]. Of these detectors, semiconductors that possess high radiation stopping power and a large carrier mobility-lifetime product tend to in principle achieve detection with superior energy resolution (ER), but this has proved extremely challenging in the past 40 years[11]. Both high-purity germanium (HPGe) and silicon (Si) are recognized as the gold standard for radiation detection due to their superior ER[12,13]. However, their applications are limited by the cooling system and the operation temperature range, respectively[14].

Therefore, many compound semiconductors have been introduced and developed for the α particles detection (Fig. 1)[9,15–24]. The good ER is achieved by GaN[25], SiC[26], and CdZnTe[27] detectors illuminated under 5.5 MeV α particles, but the broad applications are still prevented. For example, GaN and SiC struggle with low resistivity and poor uniformity, which results in high leakage current for large-size detectors. In addition, the wider band gap of GaN (3.4 eV, at room temperature, RT) and SiC (3.20 eV @ RT) leads to a larger electron-hole pair energy, which introduces more statistical fluctuations (or Fano noise). Although the commercial CdZnTe detector has achieved an ER of 0.6% at 5.5 MeV[27], it has a high manufacturing cost and unresolved growth issues. Moreover, given the environment in space and extreme conditions in nuclear facilities, an ideal α detection set-up should be sensitive and stable except the resolution. Unfortunately, the state-of-the-art CdZnTe detectors are tend to be severely damaged under high irradiation doses[28] and not able to operate at high temperatures due to the relatively narrow band gap (1.64 eV @ RT).

Recently, $CsPbBr_3$ have emerged as promising candidates for high-efficiency α particle detection, owing to their remarkable defect tolerance[29–32]. Moreover, the $CsPbBr_3$ single crystal features a wide band gap (~2.26 eV @ RT[33]), which is helpful to improve the operation temperature range compared to the Si and CdZnTe detectors. Nevertheless, the improvement of energy resolution based on $CsPbBr_3$ α particle detector is still a formidable challenge. Generally, the ER of a detector depends on the total measured variance of the observed photopeak, σ_{tot}^2, which is determined by Fano noise (σ_F^2), charge collection (σ_c^2), electronic noise (σ_{el}^2) and other elements (σ_{other}^2, such as air absorption) that cause the α particles spectrum to exhibit a low-energy tail,

$$\sigma_{tot}^2 = \sigma_F^2 + \sigma_c^2 + \sigma_{el}^2 + \sigma_{other}^2 \quad (1)$$

Several strategies have been proposed to decrease the electronic noise σ_{el}^2, which is dominated by the detector leakage current and the noise generated by the front-end readout circuit. Pan et al.[34] compared the leakage current of $CsPbBr_3$ detectors with Zr, Bi, Ti, and Ga electrodes. The results show that the Bi electrodes are recognized to achieve the highest stability. He et al.[29] reported an asymmetric electrode α particles detector based on the $CsPbBr_3$ crystal grown using the Bridgeman method, by which an ER of about 15% has been measured. Furthermore, Zhang et al.[24] used the structure of Ti/Ni/$CsPbBr_3$/Ni/Ti to obtain an ER of 5.7%. However, perovskite semiconductors combined with corresponding electronic designs have not been largely explored so far. Therefore, the specific system noise needs to be further designed to decrease the noise, since the ER of α particle detector is considerably degraded by the noise of front-end readout circuit.

In this work, we report a high energy resolution achieved by solution-grown $CsPbBr_3$ for ^{241}Am 5.5 MeV α particles. The superior performance originates from material processing and specialized application-specific integrated circuits (ASIC), which match the carrier transport behaviors of $CsPbBr_3$ for radiation detection. In particular, to reduce the dark current and optimize the crystallization quality near the contact, the as-grown crystals are thinned to decrease the $CsPb_2Br_5$ defect. The leakage current of the proposed detector is further decreased by introducing the Schottky electrode, even at high temperatures. Additionally, the measurement environments are investigated, focusing on the effects of air scattering and absorption on the α particles response. Finally, the $CsPbBr_3$ detectors response stability is investigated under high applied bias voltage with long time duration.

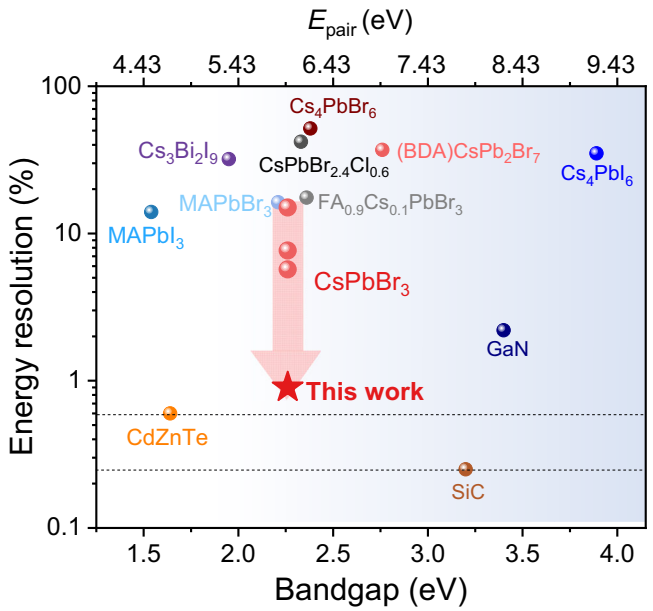

Fig. 1 | Evolution of compound semiconductors performance. Evolution of the energy resolution (^{241}Am 5.5 MeV α particles) of the best traditional compound semiconductors[25–27] and organic/inorganic perovskite detectors[9,15–24] (E_{pair} is the ionization energy, E_g is bandgap energy, $E_{pair} = 2E_g + 1.43$[20]).

Results

Low dark current and stable response of $CsPbBr_3$ detector

Generally, the perturbation of the local temperature and solution concentration is inevitable during the preparation of $CsPbBr_3$ single crystal by the inverse temperature crystallization (ITC) method[23], which leads to the formation of $CsPb_2Br_5$ defects with gradients distribution in the crystal, as shown in Fig. 2a. The $CsPb_2Br_5$ defects with polyhedral morphology embedded in $CsPbBr_3$ crystal are identified by scanning electron microscope (SEM) and energy dispersive spectrometer (EDS), as shown in Supplementary Fig. 1 and Supplementary Table 1. To further compare the SEM results before and after thinning, batches of as-grown $CsPbBr_3$ single crystals are evaluated (Supplementary Fig. 2 and Supplementary Table 2). The $CsPb_2Br_5$ defects gradually decrease as thinning, indicating that the higher concentration of $CsPb_2Br_5$ tends to be distributed near the $CsPbBr_3$ surface.

Although the two-dimensional $CsPb_2Br_5$ secondary phase has a wider bandgap than the three-dimensional $CsPbBr_3$ (Fig. 2b), the charge transport properties are usually degraded by the misfit interface and the extended defect[35,36]. The free carrier concentration, which dominates the bulk resistivity, is significantly affected by the grown-in point defects and impurities that accumulate at the interface[35]. To investigate the effects of the $CsPb_2Br_5$ defects, the electrical performances of $CsPbBr_3$ crystals are characterized. The decrease in leakage current has been proposed by thinning and polishing the $CsPbBr_3$ crystal, with the value significantly reduced from 2119.5 nA·cm^{-2} to 526.7 nA·cm^{-2} under an electric field of 1000 V·cm^{-1} (Fig. 2c), which in turn results in a resistivity >10^9 Ω·cm (Supplementary Fig. 3).

In addition, the space-charge-limited current (SCLC) technique is adopted to compare the trap densities before and after thinning. The trap density of $CsPbBr_3$ after thinning is calculated to be ~7.5×10^9 cm^{-3} according to the SCLC theory, which is lower than that of as-grown crystal (~2.7×10^{10} cm^{-3}) and other crystals[37], as seen in

https://doi.org/10.1038/s41467-024-50746-7

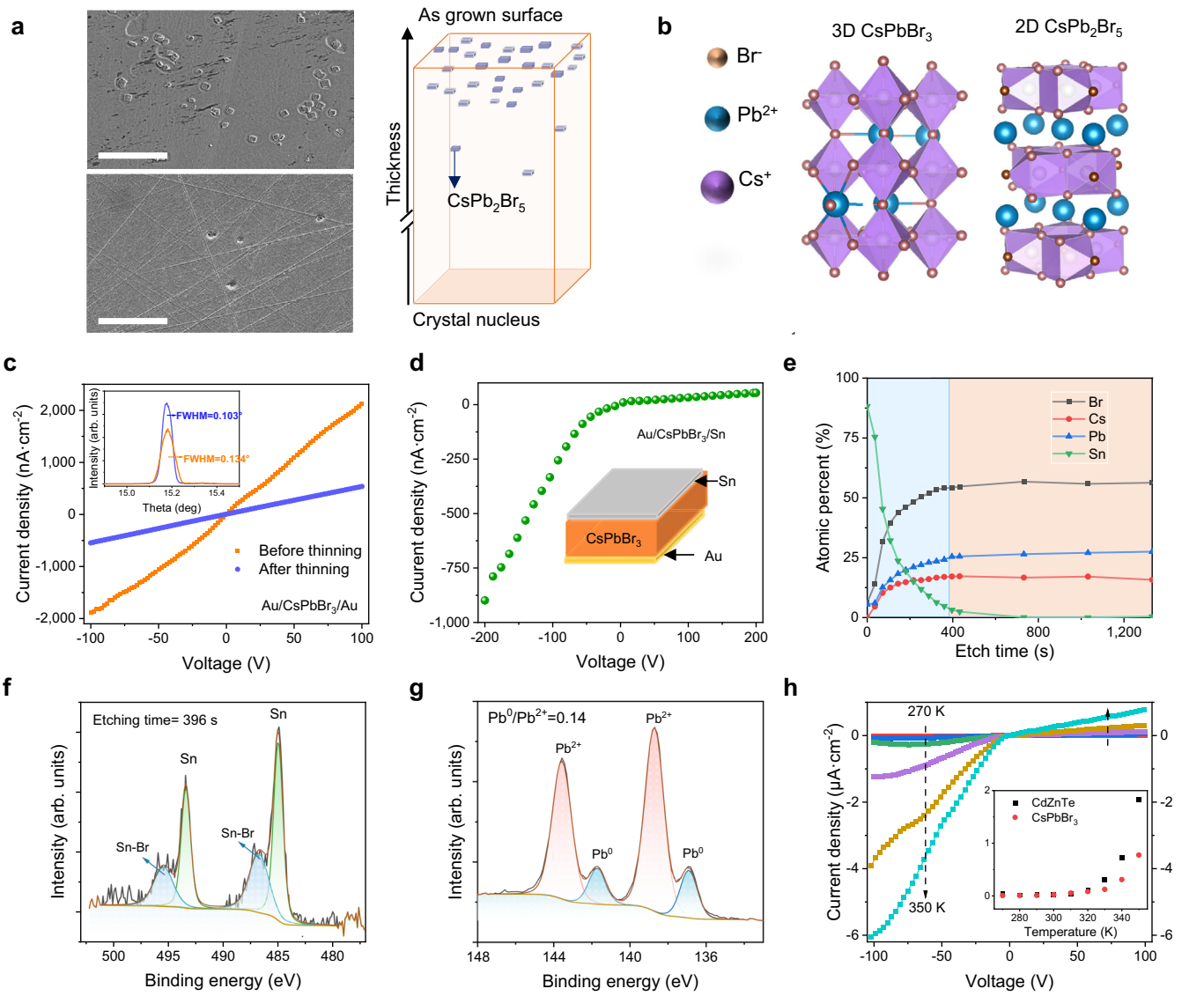

Fig. 2 | Device performance of planar $CsPbBr_3$ devices. a The $CsPb_2Br_5$ phase defects at different crystal thicknesses. The scale bars in white color are 20 μm. **b** The structure of $CsPbBr_3$ and $CsPb_2Br_5$. **c** *J-V* characteristics for the planar Au/$CsPbBr_3$/Au device (the inset is X-ray rocking curves of the $CsPbBr_3$ single crystal) before and after thinning (d = 1 mm). **d** *J-V* characteristics for the Au/$CsPbBr_3$/Sn device. **e** Atomic percentage *vs.* etching time of each element of Sn/$CsPbBr_3$. **f** X-ray photoelectron spectroscopy (XPS) with an etching time of 396 s. **g** Pb 4 f XPS spectra at the interface. **h** Temperature dependence response of the Au/$CsPbBr_3$/Sn device from 270 K − 350 K. (The inset is the comparison of leakage current between $CsPbBr_3$ and CdZnTe at different temperatures with the same electric field of 1000 V cm^{-1}).

Supplementary Fig. 4. Simultaneously, the full width at half maximum (FWHM) in the X-ray rocking curve of the $CsPbBr_3$ single crystal is obtained with a value of 0.103° after thinning, indicating superior crystallization quality compared to the as-grown $CsPbBr_3$ (0.134°). Thus, all these measurements demonstrate that the structure defects near the $CsPbBr_3$ crystal surface grown from solution are effectively suppressed by thinning.

However, the dark current density of the $CsPbBr_3$ device with the symmetric electrodes is still not satisfied for long-term operation, even after thinning (Supplementary Fig. 3). To maintain a low and stable dark current under a high bias voltage, the Schottky-type Au/$CsPbBr_3$/Sn detector is fabricated. The device with a typical *J-V* characteristic curve exhibits a low dark current density of 34.6 nA·cm^{-2} at a reverse bias voltage of 200 V (2000 V·cm^{-1}), as shown in Fig. 2d. Moreover, it should be noted that the variation of dark current is vital in maintaining high stability of $CsPbBr_3$ detector. The dark current of Au/$CsPbBr_3$/Sn detector as a function of time exhibits a small fluctuation under the reverse voltage from 2 V to 200 V (Supplementary Fig. 5), which demonstrates the better stability of $CsPbBr_3$ detector with Schottky electrode.

Additionally, the contact reaction between the electrode and the crystal should also be considered, which usually leads to the deterioration of the signal-to-noise ratio and ER[20,23,38–41]. To further evaluate the contact stability between Sn electrodes and crystals, the depth profile analysis of X-ray photo-electron spectroscopy (D-XPS) is conducted on the Sn/$CsPbBr_3$ (Supplementary Fig. 6). The variation of element atomic percentage as a function of etching time shows that the penetration of Sn into the $CsPbBr_3$ crystal is limited (Fig. 2e). In addition, the chemical state of Sn at the interface was determined, which showed a weak Sn-Br peak at 486.74 eV (Fig. 2f), indicating an inevitable reaction[38,40]. To quantify the reaction, the peak area ratio of Pb^0 and Pb^{2+} is fitted according to the corresponding redox equation[39,42,43]:

$$Pb^{2+} + 2e^- \rightarrow Pb^0 \quad (2)$$

https://doi.org/10.1038/s41467-024-50746-7

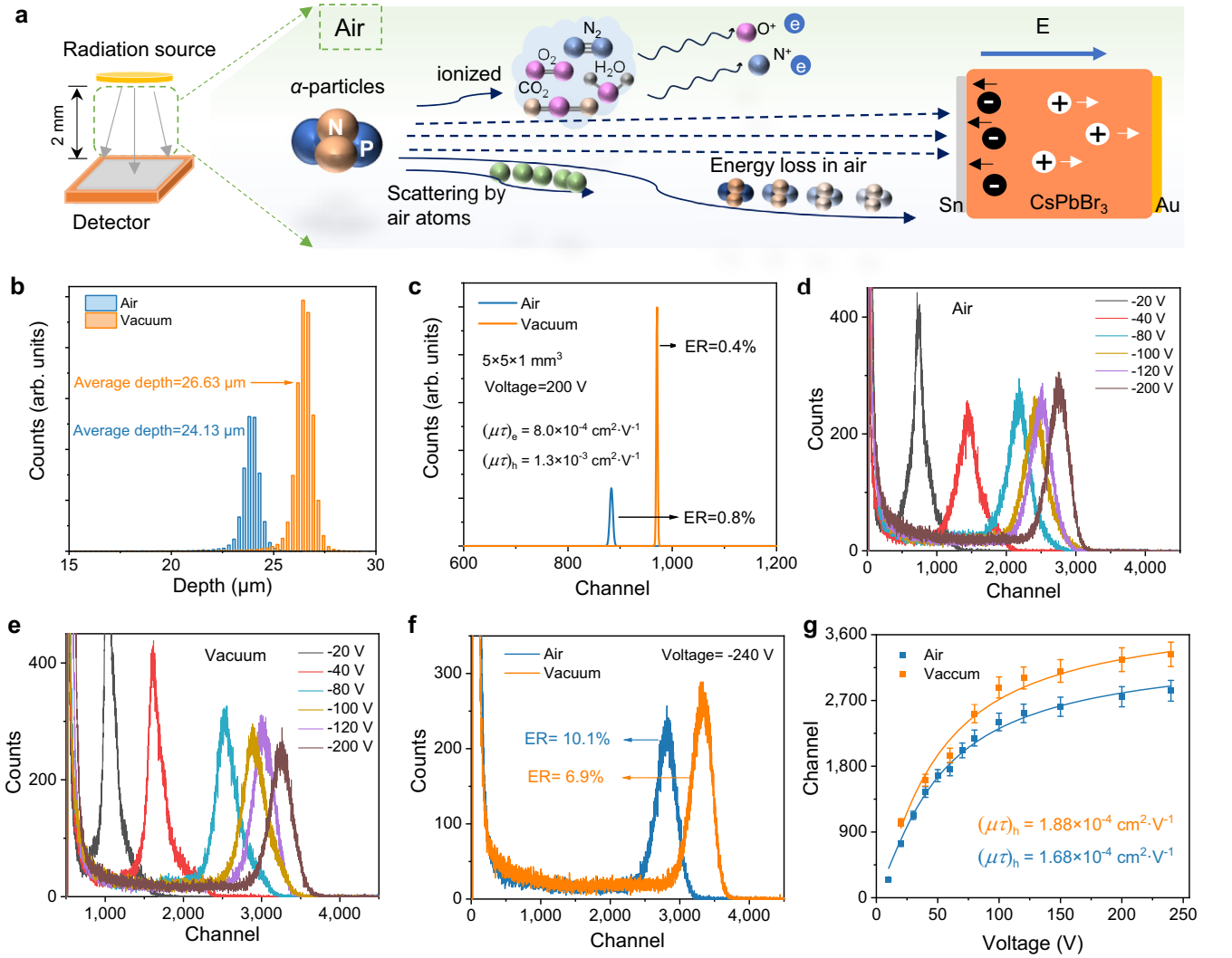

Fig. 3 | Spectral response of Au/CsPbBr$_3$/Sn detector in air and vacuum to α particles. a Schematic view of detectors in air. **b** The depth of the incident α particles by simulation. **c** The theoretical energy spectra in air and vacuum. **d**, **e** The experimental energy spectra in (**d**) air and in (**e**) vacuum. **f** The energy spectra in air and vacuum at −240 V. **g** The peak position fit to the Hecht equation. The error bars represent 5% errors from determining the channel number for air and vacuum.

The Pb^0/Pb^{2+} ratio is 0.14 for Au/CsPbBr$_3$/Sn (Fig. 2g), that is comparable to the optimized Au/Al/BCP/C_{60}/CsPbBr$_3$/Au structure[42], which demonstrates a stable contact with negligible reaction between Sn and CsPbBr$_3$.

Considering space exploration and nuclear well logging, the α particle detectors have to work at high temperatures, which injects more hot carriers and increases the current leakage. The leakage currents of commercial CdZnTe and CsPbBr$_3$ detectors are compared (Fig. 2h). The results show that the leakage current density of the CsPbBr$_3$ detector is 775 nA·cm^{-2}, which is almost one-third of the CdZnTe detector (1830 nA·cm^{-2}) under the same electric field (1000 V·cm^{-1}) at 350 K, as shown in Supplementary Fig. 7. Moreover, the current density of CdZnTe is significantly larger than that of CsPbBr$_3$ detector when the temperature is over 320 K. This indicates that the CsPbBr$_3$ detector with a relatively larger wide gap (Supplementary Fig. 8) exhibits great potential to be used in high-temperature applications.

α particles detection by CsPbBr$_3$ detector

A schematic of the α particles induced pulse height spectra by the CsPbBr$_3$ detector is shown in Fig. 3a. Generally, the energy of the particles is deposited in air in the following ways: firstly, α particles interact with CO_2 and air components (N_2, O_2), resulting in the air being positively ionized due to the loss of electrons; secondly, α particles can be scattered by the air atoms; after that, the remaining incident α particles are incident into the detector with a distance-dependent flux and energies <5.5 MeV. Therefore, the broadening (σ_{other}^2) brought by air between the source and the detector must be taken into account, especially when using an uncollimated α particles source. The mean depth of the incident α particles in CsPbBr$_3$ was calculated by Geant4 to be 26.63 μm and 24.13 μm in vacuum and air, respectively, as shown in Fig. 3b. Theoretically, the statistical fluctuation of the electron-hole pairs (E_{pair}) produced by the photoelectric interaction of α particles determines the ideal energy resolution. This fluctuation is directly proportional to the energy of the incident photon. Fano statistical limit (σ_F^2) ER of 0.077% is potentially predicted from the statistics of charge carrier formation (assuming an average value for the Fano factor of 0.1[31]), which is illustrated in Supplementary Note. However, the non-uniform charge mobilities and the de-trapping centers in the detector volume need to be considered in the experiments. Therefore, the theoretical ER for α particle is optimized from 0.8% to 0.4% by changing the environment from air to vacuum in combination with the transport performance of the CsPbBr$_3$ detector (Fig. 3c).

To compare with the simulation results, a planar $CsPbBr_3$ detector is fabricated in dimensions of $4 \times 4 \times 1.0\ mm^3$ to provide the efficiency and spectroscopic performance for α particle detection. As the range of α particles in $CsPbBr_3$ is ~24 μm whereas the detector is much thicker, the contribution of electrons to charge can be ignored when the radiation source is incident from the anode electrode. (Supplementary Fig. 9). The resulting spectra of the $CsPbBr_3$ detectors measure in air and vacuum are shown in Fig. 3d, e, respectively, illuminated by an uncollimated 5.49 MeV ^{241}Am α source. The negative bias is applied to the Au electrode while the Sn electrode was grounded. The peaks become narrower with increasing voltage, demonstrating a higher charge collection efficiency from each ionizing event. Notably, the ER is improved to 6.9% in vacuum, which is consistent with the simulation results (Fig. 3f).

Further, the mobility-lifetime product $\mu\tau$ is calculated by α particles induced pulse height spectra using Hecht equation[29,30], according to the relationship of the peak channel number versus voltage under different environments. The hole mobility-lifetime $(\mu\tau)_h$ is examined with the value of $1.68 \times 10^{-4}\ cm^2 \cdot V^{-1}$ and $1.88 \times 10^{-4}\ cm^2 \cdot V^{-1}$ in air and vacuum, respectively, which are ascribed to the less scattering in a vacuum environment and the higher energy of the incident particles (Fig. 3g). Higher hole mobility-lifetime in vacuum also increases the charge collection that further decreased the σ_c^2, resulting in better ER. Similar results are obtained for the commercial CdZnTe detector (Supplementary Figs. 10, 11), which further proves the impact of the environment on charge collection efficiency and ER.

To evaluate transport behaviors under different situations, the time-of-flight (TOF) technique[30] is employed to estimate the mobility of holes μ_h. Note that all experiments are performed after thinning since the $CsPb_2Br_5$ phases deteriorate both the rise time and mobility of the detector (Supplementary Fig. 12). The holes need to travel nearly the entire length of the crystal, and the rise time of the pulse corresponds to the drift time of the carriers. The pulse shape and the rise time of the $CsPbBr_3$ detector (normally, 10–90% single amplitude) under various applied biases are shown in Supplementary Fig. 13. For reliable statistics, a total of 5000 traces are measured for each voltage under air and vacuum, respectively, and the corresponding distribution histograms of the rise time (Fig. 4a, b) are used to calculate the hole drift time t_{dr}. The narrower rise time distributions of vacuum compared to air at the same applied voltage can be attributed to the higher mobility in vacuum conditions. The mobility μ is extracted using the expression:

$$\mu = \frac{v_{dr}}{E} = \frac{d^2}{Vt_{dr}} \tag{3}$$

where V is the bias voltage and d is the sample thickness. The resulting μ_h under the air and vacuum are $42\ cm^2 \cdot V^{-1} \cdot s^{-1}$ and $50\ cm^2 \cdot V^{-1} \cdot s^{-1}$, respectively (Fig. 4c).

These results are consistent with those of the CdZnTe detector, which further demonstrated that the resulting charge transfer performance is improved by tailoring the operation conditions (Supplementary Fig. 14). When uncollimated α particles are incident to a radiation detector, most particles are emitted at low angles. These low-angle particles have longer path than the incident particles, resulting in a greater probability of interaction with air. The ER and mobility of the hole are degraded due to the interaction of the particles with the air, resulting in energy loss. Therefore, a vacuum system for high ER $CsPbBr_3$ α spectrometer is optional that can be employed to reduce the interaction with air[26]. At the same time, our results also show that the $CsPbBr_3$ α particle detectors can be adapted to different applications and maintain high energy resolution.

Keeping high performance and stability at a high temperature is important due to the harsh thermal environment in space and terrestrial detection. To evaluate the temperature-dependent pulse height spectra of the $CsPbBr_3$ detector, the channel number of the photopeak centroid is measured at temperatures ranging from 293 K – 343 K. The $CsPbBr_3$ sustains a stable channel number, which indicates better high-temperature stability than CdZnTe in the temperature range of 293 K – 343 K (Fig. 4d). To further verify the temperature dependence of the α particle response time, the rise times of the proposed $CsPbBr_3$ detector from room temperature to 343 K are measured and shown in Fig. 4e. As reported in ref. 31, the operating temperature of the CdZnTe detector is limited to ~ 323 K (50 °C), due to the increasing electronic noise induced by the excessive hot charges at higher temperatures. By contrast, $CsPbBr_3$ has a wider band gap (Supplementary Fig. 8), which maintains a lower dark current and offers the capability of higher operational temperatures. Indeed, a small variance in the rise time of the $CsPbBr_3$ detector is observed even when subjected to 343 K at an electric field of $1000\ V \cdot cm^{-1}$, indicating that the temperature dependence of charge transport performance is negligible.

Generally, the polarization effect induced by ion migration and space charge resulting from $CsPb_2Br_5$ defects poses a significant concern for halide perovskites utilized in radiation detection, which leads to a shift of the full energy peak and deterioration of resolution[33]. The peak channel number and energy resolution maintain relative stability for the $Au/CsPbBr_3/Sn$ detector exposed to α particles during a continuous test under $1000\ V \cdot cm^{-1}$ (shaping time was 6 μs) over 12 h (Fig. 4f and Supplementary Fig. 15). In addition, the pulse height spectra of the resulting unencapsulated $CsPbBr_3$ detector show small fluctuations for over 9 months (Supplementary Fig. 16), which demonstrates the promise of robustness and stability over prolonged periods.

$CsPbBr_3$ detectors with an optimized readout electronics

The impact of electronic system noise σ_{el}^2 is another critical factor on ER that needs to be emphasized[44–46]. Since the relatively long cables used in the commonly used nuclear instruments introduce surrounding noise and parasitic capacitance, the ER is still limited, as mentioned above. Moreover, the nuclear instrument cannot match the electronic parameters with the fabricated $CsPbBr_3$ detector. Thus, a full-customized readout application-specific integrated circuit (ASIC) is designed specifically for evaluation of the as-proposed $CsPbBr_3$ detector.

As shown in Fig. 5a and Supplementary Fig. 17, one channel of the ASIC is mainly composed of a charge sensitive amplifier (CSA) and a CR-$(RC)^4$ slow shaper, which is beneficial to improve the signal-to-noise ratio and obtain a semi-gaussian wave. The CSA is adopted to amplify and convert the charges induced by particles into voltage, whose gain is determined by its feedback capacitance. In fact, the slow shaper is a band-pass filter to decrease the noise. Thus, the output amplitude of the shaper is directly proportional to the energy of the particles. Since the energy of α particles is 5.5 MeV, the maximum input charge of the readout circuit is required to be sufficiently high. The feedback capacitance of the proposed CSA is adjusted to provide two different gains. The output of the 2nd stage is connected to the chip pad to measure the higher-energy particles since each stage of the shaper provides a separate gain. Moreover, the output of the 4th stage is utilized for low-noise applications.

To match the relatively low mobility of holes in $CsPbBr_3$ crystal, the peaking time of the slow shaper is designed to be adjustable. This configuration helps to weaken the influence of ballistic deficit, thus enhancing the ER. The core amplifier built-in the slow shaper is implemented by a differential amplifier, which can improve power supply rejection to achieve low noise. Bandgap and bias circuit networks are designed on-chip to provide clean reference voltage and bias voltage for the readout circuit, resulting in a simplified measurement system. The proposed ASIC is fabricated and evaluated using standard commercial complementary metal oxide semiconductor (CMOS) processing. As shown in Fig. 5b, the

https://doi.org/10.1038/s41467-024-50746-7

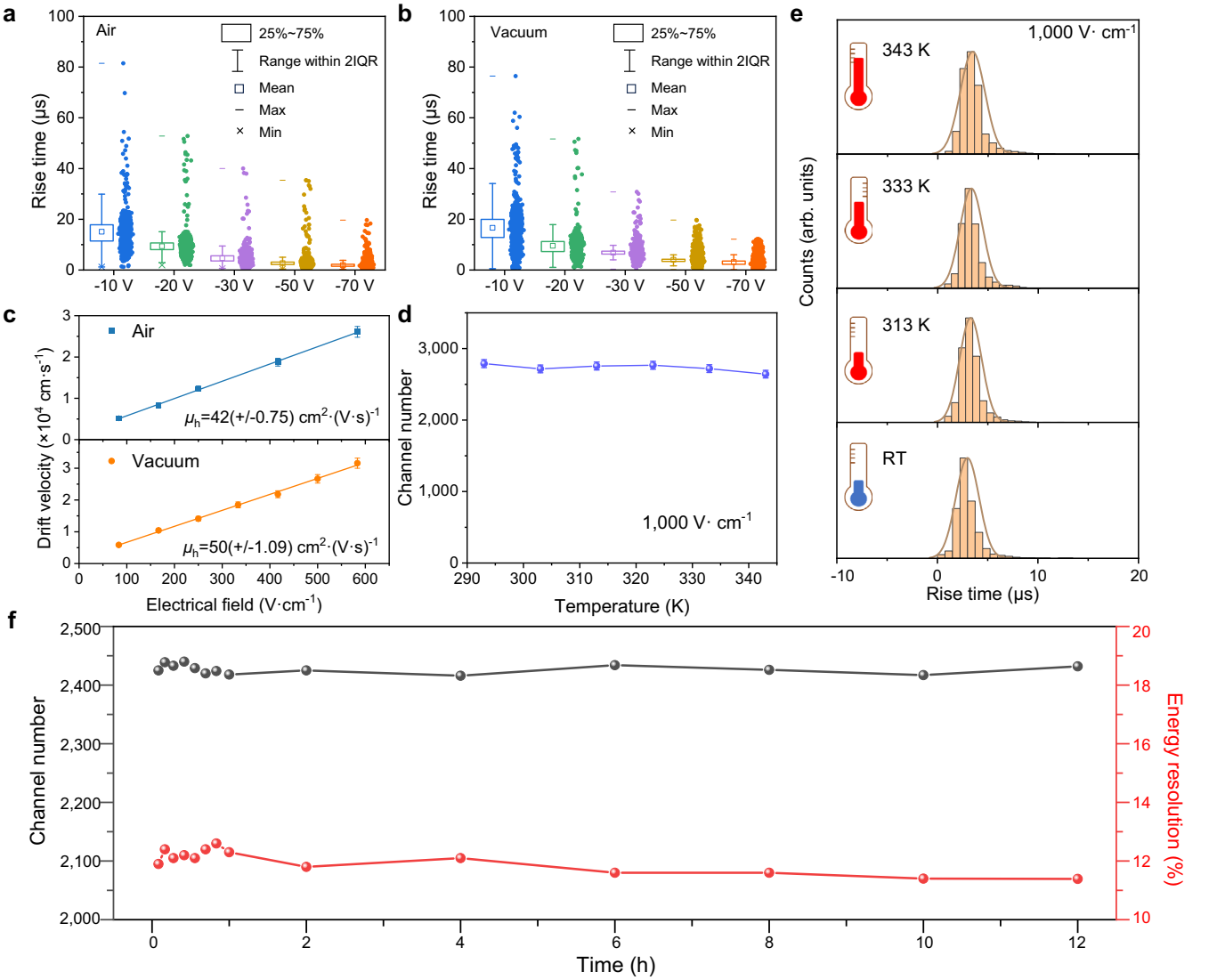

Fig. 4 | Charge transport properties in different conditions. a, **b** The distributions of the rise time for holes in (**a**) air and (**b**) vacuum. IQR is inter-quartile range. **c** The hole drifting velocities *vs.* electric field in air and vacuum, respectively. The error bars represent 5% errors. **d** The corresponding α particles channel number with different temperature for Au/$CsPbBr_3$/Sn detector. The error bars represent 2% errors. **e** The distributions of the rise time from room temperature (RT) to 343 K (70 °C). **f** The peak channel and energy resolution over a 12 h period.

amplitude of the slow shaper output voltage is monotonically increasing as the input charge increases, which tends to be saturated when the peaking time becomes larger. Thus, to decrease the die area, the resistors of the slow shaper are realized by the transistors that operate in the linear region, of which the on-resistance varies with a lower gate-source voltage. Additionally, both a maximum charge-voltage conversion gain and a minimum equivalent noise charge (ENC) of the proposed ASIC are achieved at a peaking time of ~2.5 μs (Fig. 5c, d).

The peak centroid and ER were also found to strongly depend on the peaking time. To match the peaking time, the $CsPbBr_3$ detector performance is investigated in combination with the system performance at different peak times. As indicated by the peaking time-dependent spectra in Supplementary Fig. 18, the ER is almost the same at the peaking times of 2.3 μs, 2.5 μs and 2.7 μs, which demonstrates that the charge carrier mobility of the designed $CsPbBr_3$ does not degrade the ER. However, the channel number of multi-channel analyzer (MCA) decreases at the peaking time of 3 μs. The reason is that the dynamic range, ENC and conversion gain of the designed prototype depend on the peaking time, as illustrated in Figs. 5b–d. The resulting pulse height spectra also correspond to a decrease in gain when the peaking time is 3 μs. Since the energy of α particles is decreased by the collision with air, the measured charge is lower than its ideal value.

In Fig. 5e, the designed $CsPbBr_3$ detector obtains the highest ER of 1.1% with a peaking time of 2.5 μs under ambient conditions, rivaling the ER achieved by the CdZnTe detector with the same measurement system (Supplementary Fig. 19). At the same time, different thicknesses of the $CsPbBr_3$ detector on the spectral response of α particles are shown in Supplementary Fig. 20. While thinner detectors can achieve an optimal spectral resolution of 0.9%, thinner $CsPbBr_3$ crystals are more prone to breaking due to increased surface enrichment introduced by polishing and cutting. Therefore, to ensure both energy resolution and mechanical properties, the detector thickness is not as thin as possible. Moreover, the influence of applied voltage has also been evaluated, showing that the ER deteriorates when the bias is over 100 V, which is attributed to enhanced leakage current, as shown in Fig. 5f. The high energy resolution equips $CsPbBr_3$ for broader applications in particle detection.

https://doi.org/10.1038/s41467-024-50746-7

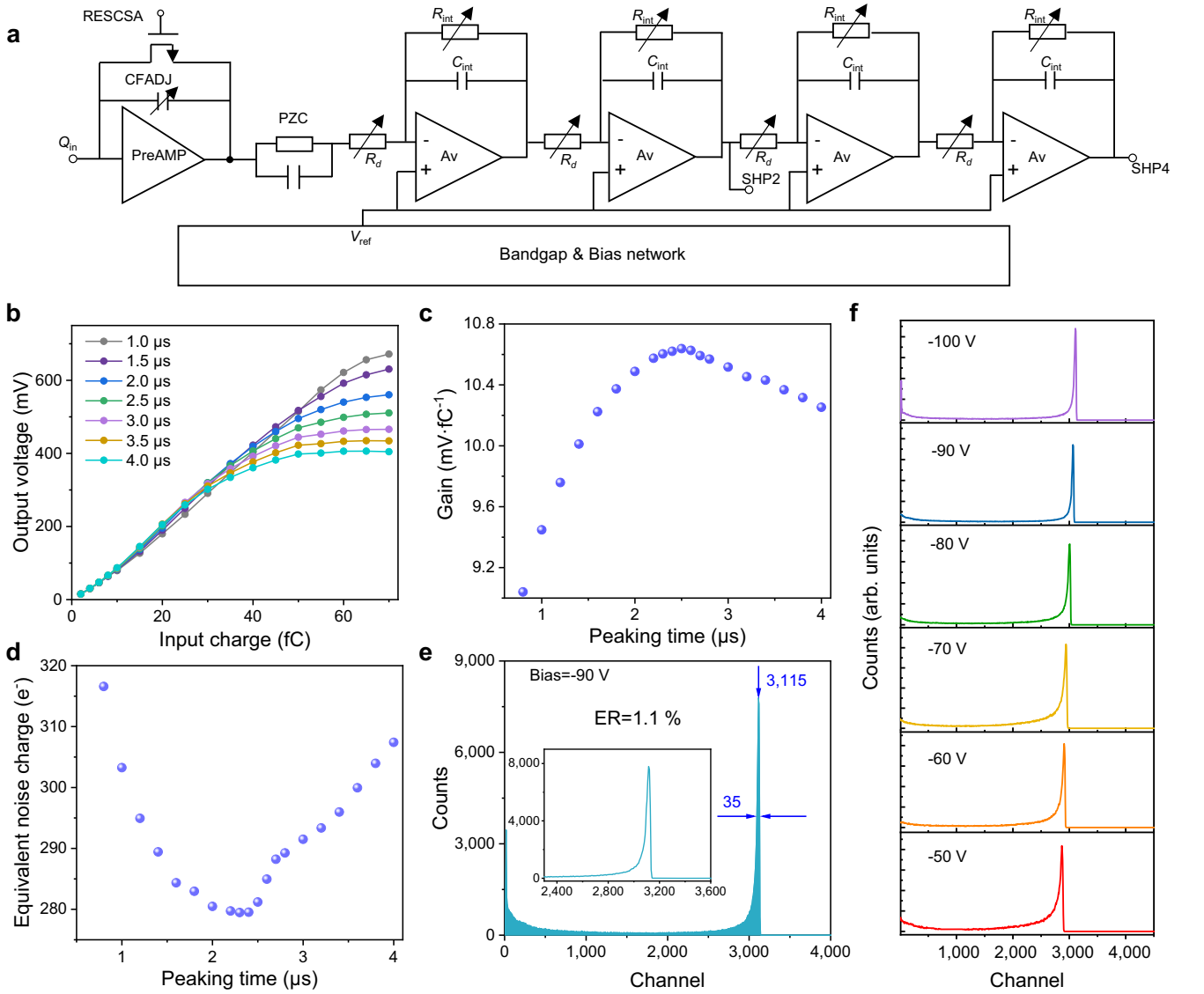

Fig. 5 | Device performance from an optimized the electronics design. a Block diagram of one channel in the readout circuit with a built-in bandgap and bias circuit. Q_{in} is input charge. PreAMP is a preamplifier. RESCSA is the bias voltage for controlling the feedback transistor. CFADJ is the voltage for adjusting the feedback capacitor. PZC is pole-zero cancellation circuit. Av is the operational amplifier. SHP is the output of each stage of the slow shaper. R_{int} is an integral resistor, C_{int} is an integral capacitor, and R_d is a differential resistor. V_{ref} is the reference voltage. **b** The amplitude output voltage of shaper V_{out} versus input charge Q_{in} at different peaking time. **c** Measured conversion gain versus peaking time. **d** Measured ENC versus peaking time. **e** α particles spectra with energy resolution of 1.1% with thickness is 1 mm. **f** α particles spectra acquired by the Au/$CsPbBr_3$/Sn detector with different applied voltage (d = 1 mm).

Discussion

In conclusion, we reported that the high resolution α particles response was achieved by the $CsPbBr_3$ detector, which is associated with both material performance and electronic design. The high crystallization quality and low leakage current were realized for $CsPbBr_3$, which is attributed to the reduction of $CsPb_2Br_5$ phase defects by thinning the crystal. The asymmetric Sn electrode was employed to further suppress the dark current density, with a value of 34.6 nA·cm^{-2} under a high electric field of 2000 V·cm^{-1}, which maintains superior temperature operation (343 K) stability than that of Si and CdZnTe. An energy resolution of the Au/$CsPbBr_3$/Sn detector for α particles was achieved as ~6.9% by reducing the air scattering. Further, a full-customized readout ASIC was designed to match the $CsPbBr_3$ detectors by considering the given material performance. Finally, the $CsPbBr_3$ detector exhibited a well-resolved spectra of 5.5 MeV α particles with spectral resolution of 1.1%. This ground-breaking advancement in energy resolution highlights the potential of the $CsPbBr_3$ single-crystal detector as an active component of novel, efficient, and new-generation α particles detection.

Methods

Crystal preparation

After the CsBr and PbBr·2DMSO mixture was dissolved in 50 mL of dimethyl sulfoxide (DMSO, ≥99.5%, Fuyu Chemical) and stirred continuously for 2 h at room temperature, the resulting solution was filtered using a 0.2 μm membrane filter. Subsequently, a 25 mL mixture consisting of dimethylformamide (DMF, ≥99%, Aladdin) and cyclohexanol (CyOH, ≥99%, Tianjin Kemiou Chemical), with a volume ratio of 1.8:1, was added to the filtered solution to prepare the precursors. The precursor solution was then immersed in a water bath. The temperature was gradually increased from 40 °C to 75 °C at a heating rate of 0.5 °C per hour[23].

Defect visualization processing

The wafer underwent chemical etching using a mixed solution of 10% HBr in ethanol for 5–30 min at room temperature[35].

α-particle spectroscopic simulation

GEANT4 was used to simulate the depth of the incident α-particles and interaction in the $CsPbBr_3$ single crystal. The configuration of the detector and the source is identical with that of the experiment section. In MATLAB, the carrier drift trace in the detector can be calculated based on the induced charge on the electrode, which is influenced by the weighting potential and the electric field. A specialized vacuum system for α particles measurements is set up with a vacuum level of 4.5–5.0 Pa.

Sample processing

The as-grown $CsPbBr_3$ crystals with thicknesses of ~1.5 mm were firstly grilled to ~1.2 mm by using 2000, 3000, 5000, and 7000 mesh sandpaper, successively. Then, the crystals were mechanically polished to ~1.1 mm with MgO powders (size of ~3 μm) in ethanol. Finally, the samples were finely polished to ~1 mm by nano-sized MgO (30 nm) with surface roughness of 2.77 nm (Supplementary Fig. 21). Note that all six sides of the crystal need to be polished. Subsequently, the polished $CsPbBr_3$ crystals were rinsed in cyclohexane and blew dried with nitrogen gas to remove surface impurities.

Device fabrication

For the fabrication of Schottky-type planar detector, the Sn and Au electrodes with thickness of 70–80 nm were deposited on the surfaces of the $CsPbBr_3$ single crystal after treatment. Typically, Sn is used as the anode, and Au is used as the cathode. After deposition, the metal electrodes (Sn and Au) were attached to the front-end readout electronics using carbon paste. To compare the performance of the proposed detector and CdZnTe detector, a detection-grade CdZnTe detector grown by the Bridgman growth was supplied by Shaanxi Imdetek Co., Ltd.

Characterization

The high-resolution X-ray diffraction rocking curves of single crystals were obtained by employing a DX-9BJ X-ray direction finder in a range of 30°–32° (2θ), with Cu $K_{\alpha 1}$ line operated at tube voltage of 40 kV and tube current of 40 mA at room temperature, respectively. The current-voltage (*I-V*) curves of $CsPbBr_3$ detectors with planar electrodes were measured under dark field. The current-time (*I-t*) curves were measured by an electrical property measurement system (Keithley 6517B), and the test was conducted with a sampling rate of 1 s per point. X-ray photoelectron spectroscopy (XPS) was performed using Al-Ka as the X-ray source. To measure the spectroscopic performance of the detector, the ^{241}Am 5.5 MeV α-particle is utilized as radiation source. During energy spectrum measurements, an eV-550 charge sensitive pre-amplifier, ORTEC 710 bias supply, ORTEC 572 shaping amplifier, and ORTEC MCA were employed.

The proposed ASIC has been fabricated in a 0.18 μm 1-Poly 6-Metal commercial standard CMOS process and the area of one readout channel is about $80 \times 900\ \mu m^2$. The prototype chip is mounted on a measuring board by package of chip on board and the $CsPbBr_3$ detector is placed close to the input of the channel in order to decrease the parasitic capacitance induced by the printed circuit board (PCB) traces and the chip package. The measuring board is put in a metal box, which protects the prototype from the influence of surrounding noise. To cover the peak energy of α particle, the output voltage of slow shaper with low gain is fed to the MCA.

Data availability

The data generated in this study are provided in the article and Supplementary Information. Additional data related to this study are available from the corresponding author upon request (xyd220@nwpu.edu.cn).

References

1. García-Torao, E. et al. Alpha-particle emission probabilities in the decay of ^{239} Pu. *Nucl. Instr. Meth. A* **334**, 477–484 (1993).
2. Onorato, G. et al. Understanding the effects of deep space radiation on nervous system: the role of genetically tractable experimental models. *Front. Phys.* **8**, 362 (2020).
3. Orfano, M. et al. Efficient radioactive gas detection by scintillating porous metal-organic frameworks. *Nat. Photonics* **17**, 672–678 (2023).
4. Gorenstein, P. et al. Detection of radon emanation from the crater Aristarchus by the Apollo 15 alpha particle spectrometer. *Science* **179**, 792–794 (1973).
5. Povinec, P. et al. Aerosol radioactivity monitoring in Bratislava following the Chernobyl accident. *J. Radioanal. Nucl. Chem.* **126**, 467–478 (1988).
6. Aumento, F. et al. Transuranium radionuclide pollution in the waters of the La Maddalena National Marine Park. *J. Environ. Radioact.* **82**, 81–93 (2005).
7. Liu, F. et al. Halide perovskites and perovskite related materials for particle radiation detection. *Nanoscale* **14**, 6743–6760 (2022).
8. Zhu, H., Liu, A. & Noh, Y.-Y. Perovskite transistors clean up their act. *Nat. Electron.* **3**, 662–663 (2020).
9. He, Y. et al. High spectral resolution of gamma-rays at room temperature by perovskite $CsPbBr_3$ single crystals. *Nat. Commun.* **9**, 1609 (2018).
10. Lee, M. M. et al. Efficient hybrid solar cells based on meso-superstructured organometal halide perovskites. *Science* **338**, 643–647 (2012).
11. Morishita, Y. et al. Organic scintillator-based alpha/beta detector for radiological decontamination. *Nucl. Instr. Meth. A* **935**, 207–213 (2019).
12. Loferski, J. et al. Radiation-damage in Ge and Si detected by carrier lifetime changes-damage thresholds. *Phys. Rev.* **111**, 432 (1958).
13. Shimaoka, T. et al. Fano factor evaluation of diamond detectors for alpha particles. *Phys. Status Solidi A* **213**, 2629–2633 (2016).
14. Tavendale, A. Large germanium lithium-drift p-i-n diodes for gamma-ray spectroscopy. *IEEE Trans. Nucl. Sci.* **12**, 255–264 (1965).
15. Xiao, B. et al. Two-dimensional dion-jacobson perovskite $NH_3C_4H_8NH_3CsPb_2Br_7$ with high x-ray sensitivity and peak discrimination of alpha-particles. *J. Phys. Chem. Lett.* **13**, 1187–1193 (2022).
16. He, Y. et al. Resolving the energy of γ-ray photons with $MAPbI_3$ single crystals. *ACS Photonics* **5**, 4132–4138 (2018).
17. Liu, X. et al. Solution-grown formamidinium hybrid perovskite $FAPbBr_3$ single crystals for alpha-particle and gamma-ray detection at room temperature. *ACS Appl. Mater. Interfaces* **13**, 15383–15390 (2021).
18. Sun, Q. et al. Optical and electronic anisotropies in perovskitoid crystals of $Cs_3Bi_2I_9$ studies of nuclear radiation detection. *J. Mater. Chem. A* **6**, 23388–23395 (2018).
19. Zhang, B.-B. et al. Ion migration controlled stability in α-particle response of $CsPbBr_{2.4}Cl_{0.6}$ detectors. *J. Phys. Chem. C.* **125**, 4235–4242 (2021).
20. Zhao, L. et al. High-yield growth of $FACsPbBr_3$ single crystals with low defect density from mixed solvents for gamma-ray spectroscopy. *Nat. Photonics* **17**, 315–323 (2023).
21. Li, Y. et al. Lead-halide Cs_4PbBr_6 single crystals for high-sensitivity radiation detection. *NPG Asia Mater.* **13**, 40 (2021).
22. Li, Y. et al. Nanosecond and highly sensitive scintillator based on all-inorganic perovskite single crystals. *ACS Appl. Mater. Interfaces* **14**, 1489–1495 (2022).

23. Wang, F. et al. Precursor engineering for solution method-grown spectroscopy-grade $CsPbBr_3$ crystals with high energy resolution. *Chem. Mater.* **34**, 3993–4000 (2022).
24. Zhang, M. et al. Metal-Semiconductor-Metal-Nanostructured $CsPbBr_3$ crystal detector for long-term stable α-particle detection. *ACS Appl. Nano Mater.* **5**, 16039–16044 (2022).
25. Xu, Q. et al. Bulk GaN alpha-particle detector with large depletion region and improved energy resolution. *Nucl. Instr. Meth. A* **849**, 11–15 (2017).
26. Park, S. et al. High resolution alpha particle spectrometry through collimation. *Nucl. Instrum. Meth. A* **784**, 470–473 (2015).
27. Amman, M. et al. Evaluation of THM-grown CdZnTe material for large-volume gamma-ray detector applications. *IEEE T. Nucl. Sci.* **56**, 795–799 (2009).
28. Šik, O. et al. Investigation of the effect of argon ion beam on CdZnTe single crystals surface structural properties. *Surf. Coat. Technol.* **306**, 75–81 (2016).
29. He, Y. et al. Perovskite $CsPbBr_3$ single crystal detector for alpha-particle spectroscopy. *Nucl. Instr. Meth. A* **922**, 217–221 (2019).
30. Zhong, H. Review of the Shockley-Ramo theorem and its application in semiconductor gamma-ray detectors. *Nucl. Instrum. Methods Phys. Res. A* **463**, 250–267 (2001).
31. He, Y. et al. $CsPbBr_3$ perovskite detectors with 1.4% energy resolution for high-energy γ-rays. *Nat. Photonics* **15**, 36–42 (2020).
32. Brenner, T. M. et al. Hybrid organic-inorganic perovskites: low-cost semiconductors with intriguing charge-transport properties. *Nat. Rev. Mater.* **1**, 15007 (2016).
33. Wang, F. et al. Low-temperature solution growth and characterization of halogen $(Cl, I)^-$ doped $CsPbBr_3$ crystals. *Cryst. Growth Des.* **20**, 1638–1645 (2020).
34. Pan, L. et al. Comparison of Zr, Bi, Ti, and Ga as metal contacts in inorganic perovskite $CsPbBr_3$ gamma-ray detector. *IEEE Trans. Nucl. Sci.* **67**, 2255–2262 (2020).
35. Cheng, Y. et al. Precursor solution-dependent secondary phase defects in $CsPbBr_3$ single crystal grown by inverse temperature crystallization. *J. Mater. Chem. A* **9**, 27718–27726 (2021).
36. Huang, Z. et al. In situ growth of 3d/2d $CsPbBr_3/CsPb_2Br_5$ perovskite heterojunctions toward optoelectronic devices. *J. Phys. Chem. Lett.* **11**, 6007–6015 (2020).
37. Cui, F. et al. Liquid-phase epitaxial growth of large-area $MAPbBr_{3-n}Cl_n/CsPbBr_3$ perovskite single-crystal heterojunction for enhancing sensitivity and stability of X-ray detector. *Chem. Mater.* **34**, 9601–9612 (2022).
38. Hao, Y. et al. Investigation of LiF interlayer on charge collection efficiency and leakage current in $CsPbBr_3$ radiation detector. *IEEE Trans. Electron. Des.* **69**, 6837–6842 (2022).
39. Zhang, L. et al. Suppressing ion migration enables stable perovskite light-emitting diodes with all-inorganic strategy. *Adv. Funct. Mater.* **30**, 2001834 (2020).
40. Li, T. et al. Understanding the interfacial reactions and band alignment for efficient and stable perovskite solar cells built on metal substrates with reduced upscaling losses. *Adv. Mater.* **35**, 2211959 (2023).
41. Xing, G. et al. Long-range balanced electron- and hole-transport lengths in organic–inorganic $CH_3NH_3PbI_3$. *Science* **342**, 344–347 (2013).
42. Chen, Z. et al. Ultrasensitive and robust $CsPbBr_3$ single-crystal x-ray detectors based on interface engineering. *ACS Appl. Mater. Interfaces* **15**, 51370–51379 (2023).
43. Wu, S. et al. A chemically inert bismuth interlayer enhances long-term stability of inverted perovskite solar cells. *Nat. Commun.* **10**, 1161 (2019).
44. Bertuccio, G. & Mele, F. Electronic noise in semiconductor-based radiation detection systems: a comprehensive analysis with a unified approach. *IEEE T. Nucl. Sci.* **70**, 2310–2321 (2023).
45. Zhang, F. et al. Characterization of the H3D ASIC readout system and 6.0 cm^3 3-D position sensitive CdZnTe detectors, *IEEE T. IEEE T. Nucl. Sci.* **59**, 236–242 (2012).
46. Owens, A. & Peacock, A. Compound semiconductor radiation detectors. *Nucl. Instr. Meth. A* **53**, 18–37 (2004).

Acknowledgements

This work was supported by the National Natural Science Foundations of China (Nos. U2032170 to Y.X. and 12341502 to J.W.). The project was also supported by the National Key Research and Development Program of China (2023YFE0206300 to Y.X.), the Natural Science Basic Research Plan in Shaanxi Province of China (2024RS-CXTD-62 to Y.X.), the ND Basic Research Funds (G2022WD to Y.X.).

Author contributions

X.Z. fabricated the devices, characterized detector performance, performed theoretical simulations and analyzed the results. Y.X., J.W., X.O., and Y.Hu conceived and supervised the project. W.J. advised on experiments. R.B. grew the single crystals. X.P. preformed the $CsPb_2Br_5$ phase experiments. Y.F. and J.W. built up α-particle testing system. Y.Hao performed the contact measurements. X.Z., J.W., B.G., Y.X., and J.L. wrote the manuscript. All authors discussed the results and commented on the manuscript.

Competing interests

The authors declare no competing interests.

Additional information

Supplementary information The online version contains supplementary material available at https://doi.org/10.1038/s41467-024-50746-7.

Correspondence and requests for materials should be addressed to Jia Wang, Xiaoping Ouyang or Yadong Xu.

Peer review information *Nature Communications* thanks the anonymous reviewer(s) for their contribution to the peer review of this work. A peer review file is available.